Materials Science & Engineering A 937 (2025) 148467

Contents lists available at ScienceDirect

Materials Science & Engineering A

journal homepage: www.elsevier.com/locate/msea

Achieving grain refinement and strength enhancement of 2025 aluminum alloy by introducing a novel Al-TCB master alloy

Zhan Liu [a], Jinfeng Nie [a,*], Yuyao Chen [a,**], Kaixuan Zhou [a], Ruisheng Zhang [a],
Yonghao Zhao [a,b,***], Chong Li [c], Xiangfa Liu [d]

[a] *Nano and Heterogeneous Materials Center, School of Materials Science and Engineering, Nanjing University of Science and Technology, Nanjing, 210094, China*
[b] *School of Materials Science and Engineering, Hohai University, Changzhou, 213200, China*
[c] *State Key Laboratory of Hydraulic Engineering Intelligent Construction and Operation, School of Materials Science & Engineering, Tianjin University, Tianjin, 300354, China*
[d] *Key Laboratory for Liquid–Solid Structural Evolution and Processing of Materials, Ministry of Education, Shandong University, Jinan, 250061, China*

ARTICLE INFO

Keywords:
Grain refinement
Nucleation mechanism
Microstructure evolution

ABSTRACT

In this study, the Al-TCB master alloy was incorporated into Zr-containing 2025 Al alloys through casting metallurgy. Subsequent hot extrusion and T6 heat treatment were employed to optimize the microstructure and improve the comprehensive mechanical properties. The results show that the average grain size of Zr-containing 2025 alloy was refined from 423 μm to 96 μm by adding 2 wt% of Al-TCB master alloy. The Al-TCB master alloy has a substantial anti Zr-poisoning effect. The B-doped TiC particles induced by the Al-TCB master alloy remained stable in the Al melt, serving as an effective heterogeneous nucleation substrate. After hot extrusion and T6 treatment, the ultimate tensile strength of the 2025-2 wt% Al-TCB alloy reaches 400.0 MPa and an elongation to failure of 20.0 %. The enhancement in mechanical properties is attributed to the effective grain refinement facilitated by the Al-TCB master alloy, which also suppressed coarse-grain structure formation during the aging process.

1. Introduction

The heat-treatable Al-Cu alloy are highly competitive and attractive structural materials in transportation, aerospace and marine applications due to their combination of lower density and higher strength [1–3]. As an Al-Cu series alloy, 2025 aluminum alloy is a typical representative material employed in the fabrication of fixed/variable-pitch propeller assemblies [4,5]. The 2025 alloy offers comparable mechanical properties at a lower cost compared to fiber-reinforced polymer composites [6–8]. Conventional manufacturing routes for aluminum products include casting, extrusion, rolling, and forging [9]. However, because of the variation in undercooling during solidification, cast ingots frequently display casting defects such as excessive grain sizes, coarse dendrites, porosity, shrinkage cavities, and element segregation [10,11]. These defects severely reduce the ductility and fracture toughness, and these defects are challenging to eliminate with further heat treatment. Thus, to minimize casting defects and achieve the desired mechanical performance of the alloy, microalloying, grain refinement and deformation treatment required [12–14].

Generally, transition metal element Zr is added as an important trace alloying element (with addition of 0.1–0.3 wt%) in 2xxx and 7xxx series Al-alloys due to it can generate primary Al_3Zr particle which is coherent with the Al matrix and thermally stable at elevated temperatures [15–17]. During solidification, Al_3Zr particle can serve as a heterogeneous nucleation site, refining the grains of alloy [18]. According to Ebrahimi et al., Zr addition to an Al-Zn-Mg-Cu alloy reduced the average grain size by 23 % and the recrystallization area fraction by 65 %, improving the comprehensive mechanical properties [19]. Moreover, Zr can also hinder the recrystallization of the aluminum alloy during subsequent processing and heat treatment [20,21]. For example, Deng et al. reported that the recrystallization and grain growth were significantly inhibited in solid solution-treated Zr containing (0.08 %) Al-Cu-Li-Mn

---

* Corresponding author.
** Corresponding author.
*** Corresponding author. Nano and Heterogeneous Materials Center, School of Materials Science and Engineering, Nanjing University of Science and Technology, Nanjing, 210094, China.
E-mail addresses: niejinfeng@njust.edu.cn (J. Nie), chenyuyao@njust.edu.cn (Y. Chen), yhzhao@njust.edu.cn (Y. Zhao).

https://doi.org/10.1016/j.msea.2025.148467
Received 3 November 2024; Received in revised form 14 April 2025; Accepted 7 May 2025

alloys, and then improving the strength and ductility of this alloy [22]. Furthermore, Bansal et al. reported that the segregation of Zr atoms at the θ'/α-Al interface increases the kinetic and thermodynamic barriers to precipitate coarsening in Al-Cu alloy [16].

Grain refinement has become an essential metallurgical procedure in aluminum foundries world-wide, providing improved mechanical properties, enhanced fluidity, reduced segregation, and decreased hot crack propensity [23,24]. Commercial refiners, such as the Al-Ti-B and Al-Ti-C master alloys, effectively turn coarse columnar grains into fine equiaxed grains by introducing more heterogeneous nucleation sites [25,26]. Regarding heterogeneous nucleation of Al-Ti-B refiner, Fan et al. utilized high-resolution electron microscopy to observe that a two-dimensional compound (2DC), $TiAl_3$ forms at the interface between TiB_2 and α-Al. The orientation relationship (OR) between these phases is given by "(0001) [11$\bar{2}$0] TiB_2//(112) [$\bar{2}$01] $TiAl_3$-2DC//(111) [0 $\bar{1}$ 1]Al" [27,28]. In this interfacial structure, the formation of $TiAl_3$-2DC significantly reduces the lattice mismatch, thereby substantially increasing the nucleation potency of TiB_2 for α-Al [29]. However, it has been demonstrated that the grains of Zr-containing Al alloys are usually difficult to refine using the Al-Ti-B grain refiners [30,31]. The effectiveness of such grain refiners is severely compromised when a few hundred ppm of Zr is present in the Al melt, and this phenomenon is referred to as Zr-poisoning [32,33]. Spittle and Sadli found that adding Al-5Ti-1B grain refiner to commercial purity Al resulted in coarser grains when Zr was present with other solute elements such as Fe or Si [34]. Rao et al. found that Zr had a detrimental effect, specifically a poisoning effect, on the grain refining capability of Al-5Ti-1B [33]. It was revealed that the presence of Zr in Al melts leads to the dissolution of the nucleating substrates of $TiAl_3$-2DC and the formation of Ti_2Zr-2DC, and then impede the heterogeneous nucleation [29,35]. As an effective grain refiner, the dispersed TiC particles in Al-Ti-C master alloy display improved dispersion characteristics compared to the agglomeration-prone TiB_2 particles in Al-Ti-B master alloy [36]. However, the refining efficiency of Al-Ti-C master alloy decreases in Zr-containing alloys due to the thermodynamic instability of TiC within the aluminum matrix [32]. At refinement temperature (~720 °C), TiC particles will evolve to be Al_4C_3 phase in Al melt [37]. Given that Zr acts a crucial trace strengthening element in certain Al-Cu alloys, their grain refinement is both necessary and urgent. Therefore, new strategies to overcome Zr-poisoning, particularly for Zr-containing Al alloys, are the key directions for grain refiners to achieve breakthroughs. The Al-TCB master alloy has emerged as an effective refiner for α-Al, as it contains both B-doped TiC and C-doped TiB_2 particles [15,38,39]. Yang et al. reported that the Al-TCB master alloy performs better on grain refinement for Zr-containing 7050 Al alloy than conventional Al-5Ti-1B or Al-5Ti-0.2C due to the high efficiency of B-doped TiC particle [40]. This enhanced grain refiner significantly refines the α-Al and reduces dendrite formation. In the Al-Si melt, B-doped TiC transforms into C-doped TiB_2 due to the high level of Si, which acts as an effective nucleation substate for α-Al and overcome Si-poisoning [35,41]. However, the refinement effect of Al-TCB alloy on Zr-containing Al-Cu alloys has rarely been reported up to now. The application of a novel Al-TCB master alloy is anticipated to overcome the Zr-poisoning problem. In the present work, trace Zr with an addition of 0.1 wt% was added to the 2025 alloy to investigate the effect of Al-TCB master alloy on grain refinement and mechanical properties. Extrusion is an economical processing route that can further refine the grain, resulting in superior initial mechanical properties [22]. Furthermore, subsequent heat treatment can enhance the mechanical properties of alloy. During the aging process of 2025 alloy, a precipitation phase transformation occurs: supersaturated solid solution (SSS) → Guinier-Preston (GP I) → GP II (θ'') → θ'-Al_2Cu→ θ-Al_2Cu, which significantly affects the mechanical properties of the alloy [42].

Table 1

Nominal composition of the 2025 base alloy (wt.%).

Samples	Cu	Si	Mn	Zr	Al
Zr-free 2025	4.5	0.8	0.8	0	Bal.
Zr-containing 2025	4.5	0.8	0.8	0.1	Bal.

Table 2

Composition of the 2025 under different refinement conditions (wt.%).

Samples	2025 alloy	Al-Ti-B	Al-TCB
Zr-free 2025	100	0	0
Zr-free 2025-0.2 wt% Al-Ti-B	99.8	0.2	0
Zr-free 2025-0.2 wt% Al-TCB	99.8	0	0.2
Zr-containing 2025	100	0	0
Zr-containing 2025-0.2 wt% Al-Ti-B	99.8	0.2	0
Zr-containing 2025-2 wt% Al-Ti-B	98	2	0
Zr-containing 2025-0.2 wt% Al-TCB	99.8	0	0.2
Zr-containing 2025-2 wt% Al-TCB	98	0	2
Zr-containing 2025-4 wt% Al-TCB	96	0	4

In this work, the influence of Al-TCB master alloy on the grain refinement, microstructure and mechanical properties of 2025 alloy was investigated. The nucleation process, grain refinement mechanisms of the Al-TCB master alloy in the 2025 Al alloy melt were analyzed. The microstructure and mechanical properties of 2025-TCB alloy were further optimized through heat treatment, and the strengthening mechanisms of 2025-TCB alloy were revealed in depth.

2. Materials and method

2.1. Preparation of the 2025 alloy

The 2025 alloy used in this paper was prepared through the melting pouring process at Shandong Aluminum Magnesium New Material Co., LTD. First, a pure Al ingot (purity 99 %) was heated to 720 °C in a crucible until melted. Subsequently, electrolytic Cu (purity 99 %), pure Mn (purity 99 %), pure Si (purity 99 %) and pure Zr (purity 99 %) were added in exact amounts. The chemical compositions of 2025 alloy are shown in Table 1. The mixture was then held at 720 °C for 20 min. After complete melting, a predetermined amount of the Al-2Ti-0.3C-0.2B master alloy (hereafter Al-TCB master alloy) containing TCB complex was introduced. The content of TCB particles within the Al-TCB master alloy is approximately 2.14 wt%. The melt was stirred with a graphite rod for 10 s, kept for 20 min, and then poured into a copper mold to obtain 2025 ingots with varying grain refiner contents. In addition, 2025 ingots containing 0.2 wt% and 2 wt% Al-5Ti-1B commercial grain refiner were prepared for comparison under the same melt conditions. The Zr-containing 2025-TCB alloys with 0 %, 0.2 wt% and 2 wt% Al-TCB master alloys were then subjected to hot extrusion (extrusion process was performed at 400 °C with extrusion ratio of 20:1) and T6 treatment (solution treatment at 540 °C for 4 h and aging at 175 °C for 8 h). The as-extruded and T6-treated alloys are denoted as EXT and T6, respectively. The grain refiner contents of all alloys are presented in Table 2.

2.2. Microstructure characterization

In this experiment, Bruker-AXS D type advanced X-ray diffractometer was used to test at 40 kV, the scanning angle range was 10°–90°, and the scanning step was 0.01°. The grain structure was observed by a polarizing optical microscope. Quanta 250F field emission environmental scanning electron microscope (equipped with EDS) was used to observe the microstructure at 15 kV. Electron back scattered diffraction (EBSD) technique was used to observe the grain morphology and crystal orientation at 15 kV, and the scanning step was set to 0.5 mm. FEI Tecnai G2-20 was used to capture bright field images at 200 kV. The typical interface between the nucleation substrate and α-Al matrix was observed using a high-resolution transmission electron microscope (HRTEM). The sample was prepared by focused ion beam scanning electron

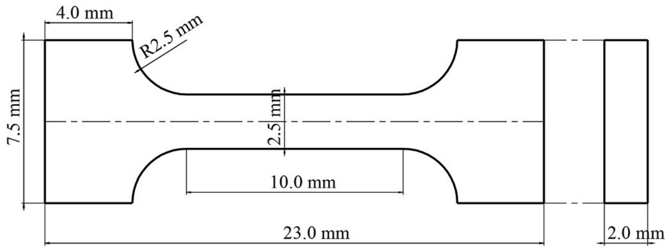

Fig. 1. Schematic geometries of tensile specimens.

microscopy. In addition, high-resolution atomic images were captured using Tian G2 60–300, which operates at 300 kV. All samples were ground and polished according to the standard process of metallography. The samples were anodized before optical observation to make the grains visible. The sample surface is further treated with electrolytic polishing with an electrolyte containing 30 vol% HNO_3 and 70 vol% CH_3OH at −25 °C before EBSD testing. TEM samples were prepared by ion thinning technique (device PIPS Gatan 695).

2.3. Mechanical properties test

The Vickers hardness test was performed using the HMV-G 21DT with an applied load force of 980.7 mN and a duration time of 15 s. At least fifteen points were measured for each specimen. The tensile property test was carried out using the LFM-kN electronic universal tensile testing machine. The samples for room temperature tensile property test were machined into "dog-bone" type bars with a gauge dimension of 10 mm × 2.5 × 2.0 mm^3 as shown in Fig. 1. Before the tensile test, the surface of each specimen was polished using 600# and 1000# sandpaper to remove traces from the electric spark wire cutting. During the tensile testing, the strain rate was controlled at 1×10^{-3} s^{-1}. To ensure the reliability of the experimental results, each test was repeated three times.

3. Results

3.1. Microstructure characterization of the Al-TCB master alloy

Fig. 2 shows the morphology and distribution of particles in the Al-TCB master alloy used in this study. Both micron and nano-scale particles are uniformly dispersed in the Al matrix, and there is no obvious agglomeration in the alloy, as shown in Fig. 2a. The XRD shows that the Al-TCB master alloy contains Al, TiC and TiB_2 (Fig. 2b). The magnified SEM images and corresponding EDS results (Fig. 2c–e) further confirm the formation of doped particles containing Ti, C and B elements. According to our previous work [35], the doped particles are B-doped TiC and C-doped TiB_2, respectively.

3.2. Microstructure characterization of the 2025-TCB with different Al-TCB addition

The average grain size and microstructure of the 2025 ingots under different refinement conditions are shown in Fig. 3. The detailed data of corresponding average grain sizes are listed in Table 3. The as-cast grains in the Zr-free 2025 alloy are very coarse, with an average grain size of 491 μm (Fig. 3a). The average grain size of Zr-free 2025 alloy can be reduced from 491 μm to 103 μm and 75 μm by 0.2 wt% Al-5Ti-1B and 0.2 wt% Al-TCB, respectively (Fig. 3b and c). As shown in Fig. 3d, Zr-containing 2025 alloy exhibits an average grain size of 423 μm, characterized by coarse dendritic structures within the grains. As is well known, Al-5Ti-1B is difficult to refine the Zr-containing Al alloy. The average grain size of Zr-containing 2025 alloy can only be slightly reduced from 423 μm to 400 μm and 327 μm by 0.2 wt% and 2 wt% Al-

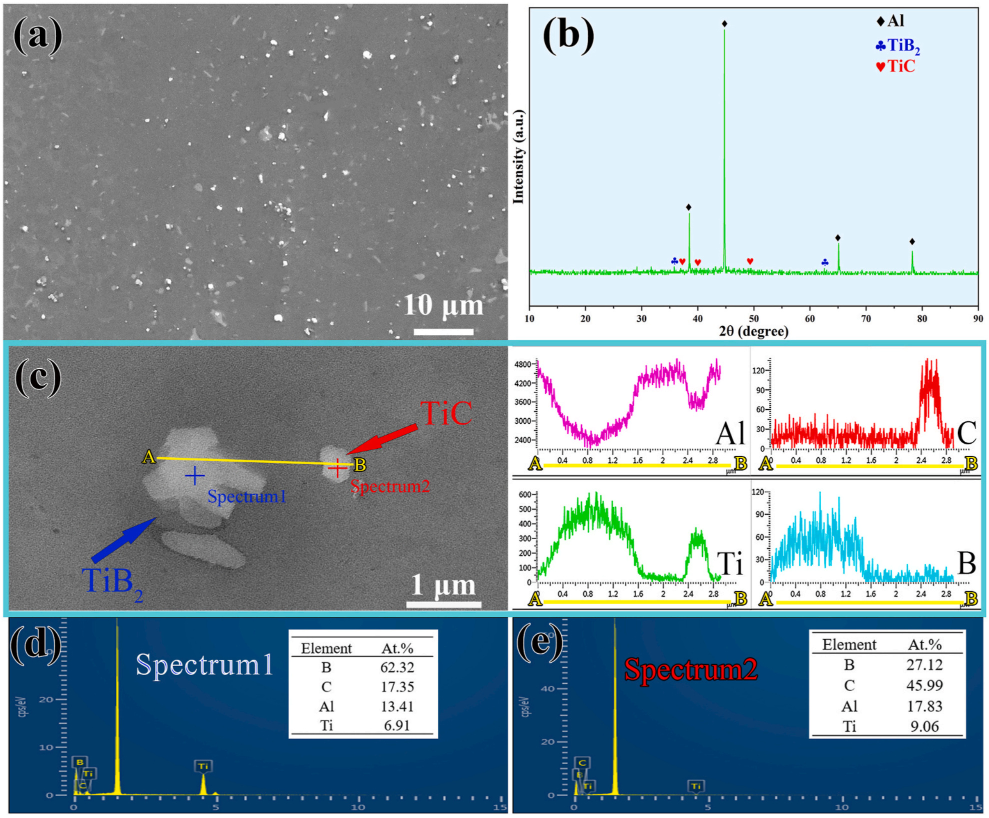

Element	At.%
B	62.32
C	17.35
Al	13.41
Ti	6.91

Element	At.%
B	27.12
C	45.99
Al	17.83
Ti	9.06

Fig. 2. Microstructure of Al-TCB master alloy: (a) the distribution of the particles; (b) the XRD results; (c) typical SEM images and EDS line-scanning patterns of the particles; (d) the quantitative analysis of TiB_2 in Fig. 2c; (e) the quantitative analysis of TiC in Fig. 2c.

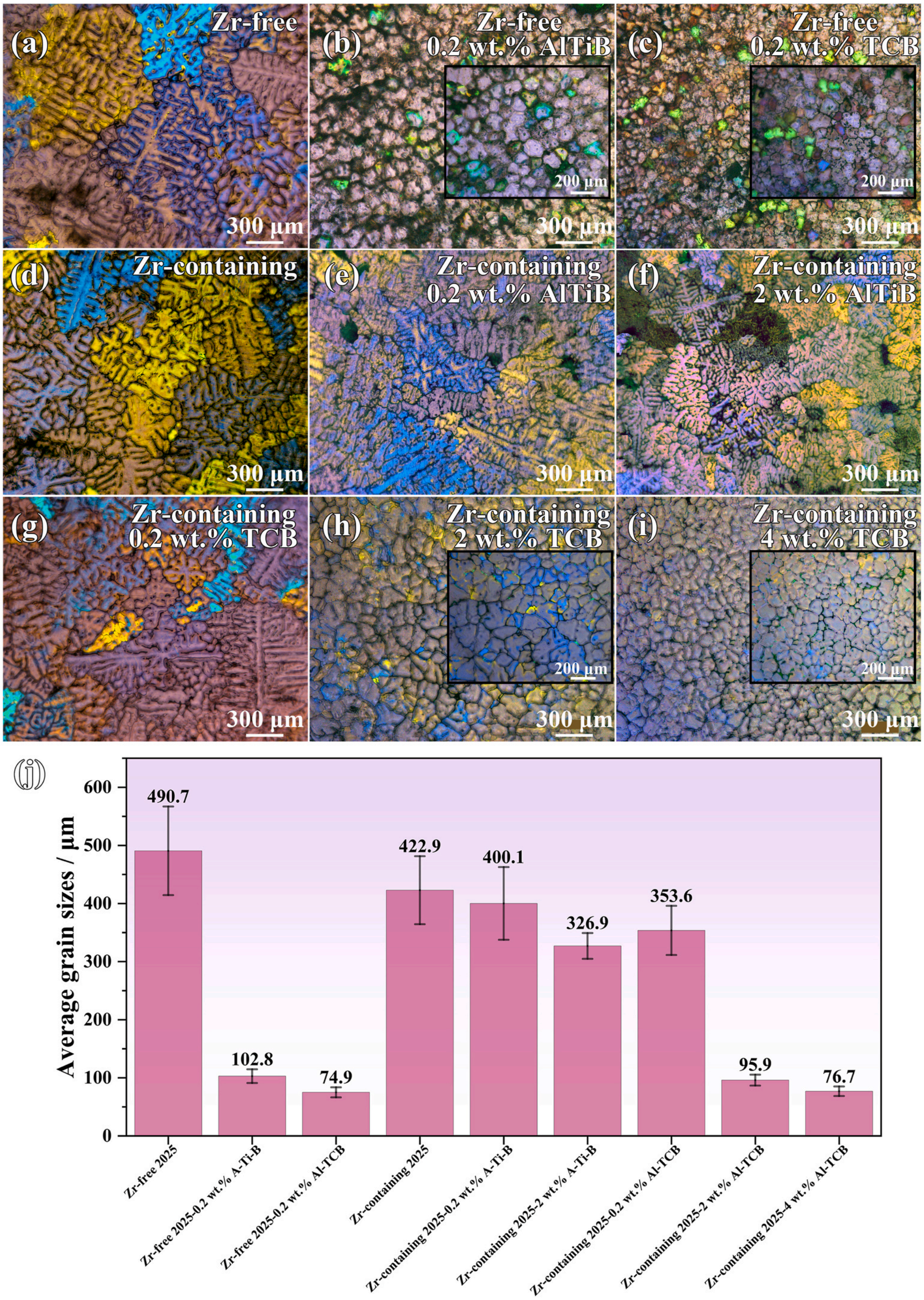

Fig. 3. Polarized light photographs and average grain size of 2025 ingots with different grain refiners contents: (a–c) Zr-free 2025 alloy, (a) adding no grain refiner; (b) adding 0.2 wt% Al-Ti-B; (c) adding 0.2 wt% Al-TCB. (d–i) Zr-containing 2025 alloy:(d) base alloy; (e) adding 0.2 wt% Al-Ti-B; (f) adding 2 wt% Al-Ti-B; (g) adding 0.2 wt% Al-TCB; (h) adding 2 wt% Al-TCB; (i) adding 4 wt% Al-TCB; (j) average grain size of α-Al under different refinement conditions.

5Ti-1B, respectively (Fig. 3e and f), which indicates the grain refinement efficiency degraded due to the Zr induced poisoning effect. By contrast, the average grain size of the Zr-containing 2025 alloy can be refined to 354 μm and 96 μm by the Al-TCB master alloy under the same condition (Fig. 3g and h), indicating that the element-doped particles show a strong grain refinement efficiency and anti Zr-poisoning potency. It shows that the Al-TCB master alloy has a significant anti Zr-poisoning effect in the present condition. The incorporation of the Al-TCB master alloy into the Zr-containing 2025 alloy increases the number of nucleation sites within the Al melt, which refines the grains and suppresses dendritic formation [35]. The average grain size is reduced to 77 μm by increasing the content of Al-TCB master alloy to 4 wt% (Fig. 3i). Despite doubling the Al-TCB master alloy addition, grain refinement improves by only around 19 %, indicating that the Al-TCB master alloy has reached its grain refinement limit at this concentration.

The microstructure of the 2025-TCB ingots was further characterized by SEM and EDS. Fig. 4 (a-d1) presents SEM images of 2025 Al alloy with varying Al-TCB master alloy contents. As shown in Fig. 4a and a1, the 2025 alloy has coarse grains with noticeable dendritic structures. According to the EDS mapping (Fig. 4e1-e4), the white phase is predominantly made up of Al and Cu elements. It has been demonstrated that Cu exhibits pronounced segregation at grain boundaries, and the

Table 3
Average grain sizes of the 2025 alloys under different refinement conditions.

Alloys	Refinement conditions	Average grain size (μm)
Zr-free 2025	none	491 ± 76
	0.2 wt% Al-5Ti-1B	103 ± 12
	0.2 wt% Al-TCB	75 ± 9
Zr-containing 2025	none	423 ± 58
	0.2 wt% Al-5Ti-1B	400 ± 62
	2 wt% Al-5Ti-1B	327 ± 22
	0.2 wt% Al-TCB	354 ± 42
	2 wt% Al-TCB	96 ± 9
	4 wt% Al-TCB	77 ± 8

concentration of Cu atoms was higher closer to the boundary [43,44]. Simulation results of Ren et al. also showed that Cu tended to segregate at pure aluminum grain boundaries, and the segregation energy was most negative at the interstitial position [45]. Under constant total Cu content, an increase in grain boundary amount may lead to the total Cu concentration at grain boundaries greater than that within the Al matrix. During the solidification process, $L(\text{liquid}) \rightarrow \alpha(\text{Al}) + \theta(\text{Al}_2\text{Cu})$ took place [46]. In this study, the addition of the Al-TCB master alloy efficiently promoted equiaxed grain formation, increased the number of grain boundaries, and greatly inhibited dendrite growth [47]. Massive Al_2Cu is distributed along the grain boundaries, resulting a network structure in Fig. 4(a–d). The transformation of coarse grains to equiaxed grains in the 2025 alloy is consistent with the polarized light photographs. The secondary phase composed of Al, Si, and Mn is also formed and is identified to be the AlSiMn secondary phase, as shown in Fig. 4 (f-f3). Meanwhile, the AlSiMn secondary phase is dispersed along the grain boundaries, which is similar with Al_2Cu. The formation of these secondary phases can be attributed to compositional fluctuations during the solidification process, which occur when the concentration of the Cu, Si and Mn elements exceeds their solubility in the Al matrix.

Good nucleation substrates of α-Al grains enhance grain refining in Al alloy. The nucleation substrates of α-Al grains in the 2025 alloy are observed, as shown in Fig. 5a–c. And Fig. 5 (b1) illustrate the distribution of Ti, B, C, and Al elements in Fig. 5b. The EDS quantitative analysis of nucleation site is given in Fig. 5c. It is confirmed that the particle is primarily composed of Ti, B and C elements. The particle is identified as B-doped TiC according to Fig. 2, which could act as a nucleation substrate for the 2025 alloy [15,41].

Analyzing the interfacial relationship between the nucleating substrate and the Al matrix aids in understanding the grain refinement mechanism of the 2025 alloy. Fig. 6 shows the HADDF-STEM image and EDS analysis of the B-doped TiC. The EDS line-scanning patterns depicted in Fig. 6a reveal a ladder-like distribution of Al and Ti elements at the interface between the B-doped TiC particle and Al matrix. EDS line-scanning includes measurements of both the Al matrix and the B-doped TiC, resulting in a continuous gradient at the interface. It is worth noting that a peak in the line-scanning patterns (red rectangle) of element B in Fig. 6a. The cause for this peak could be that the element B has somewhat enhanced on the surface of TiC particles. Both the EDS line scanning results and EDS mapping analysis prove that Zr has not aggregated at the interface of B-doped TiC/Al. Furthermore, Fig. 6c demonstrates a specific orientation relationship between the B-doped TiC and the Al matrix. Local FFT images within the purple and blue rectangle in Fig. 6c are presented in Fig. 6d and e, respectively. The Ti atoms are shown with red dots, while the Al atoms are denoted with blue dots. The B-doped TiC has an orientation relationship with Al matrix: $[112]_{\text{B-doped TiC}}//[110]_{\alpha\text{-Al}}$; $(220)_{\text{B-doped TiC}}//(\bar{1}\,1\bar{1})_{\alpha\text{-Al}}$.

3.3. Microstructures of 2025-TCB alloys after hot-extrusion and T6 treatment

Fig. 7 shows the microstructure of the extruded and T6 treated 2025-TCB alloys along the extrusion direction. Fig. 7(a–c) indicate that the extruded alloy contains two phases. EDS mappings reveal that phases are primarily composed of Cu, Si and Mn elements, which are identified as Al_2Cu and AlSiMn secondary phase [48]. It has been reported that the Al_2Cu and AlSiMn secondary phases are generated during the casting process (as shown in Fig. 4) and their morphology can be improved after heat treatment [49,50]. The Al_2Cu secondary phase appears as dot-like

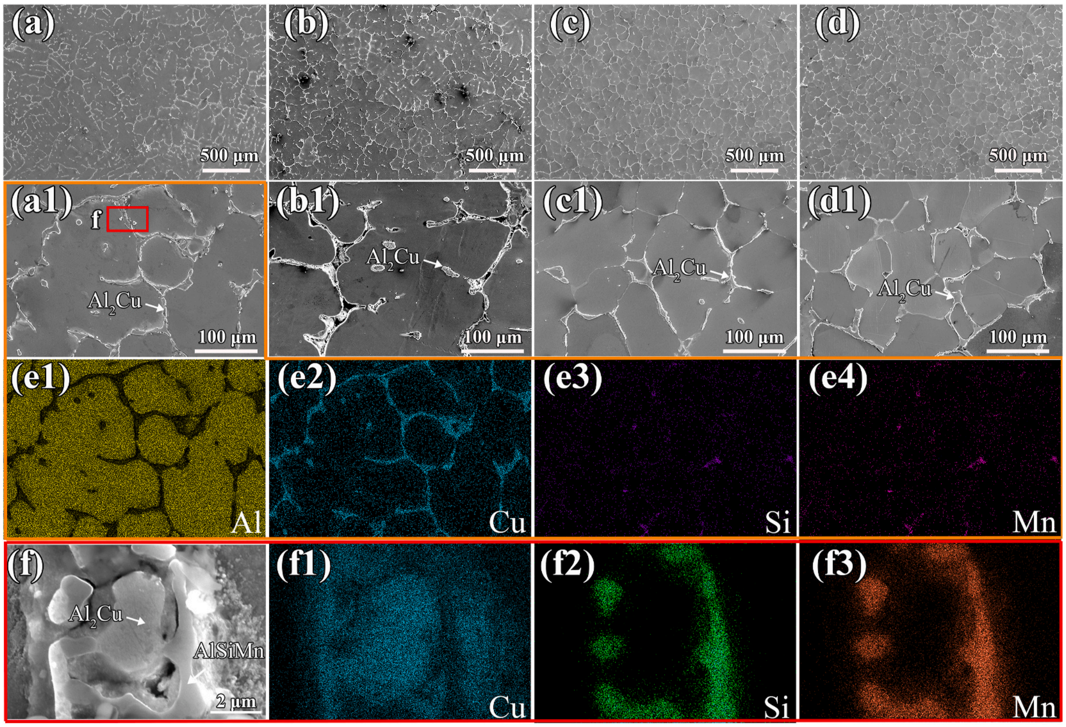

Fig. 4. Microstructures of 2025-TCB ingots with different Al-TCB contents: (a-a1) 2025 base alloy without Al-TCB; (b-b1) adding 0.2 wt% Al-TCB; (c-c1) adding 2 wt % Al-TCB; (d-d1) adding 4 wt% Al-TCB; (e1-e4) EDS mappings of the (a1); (f-f3) morphology and EDS mappings of AlSiMn secondary phase of the (a1).

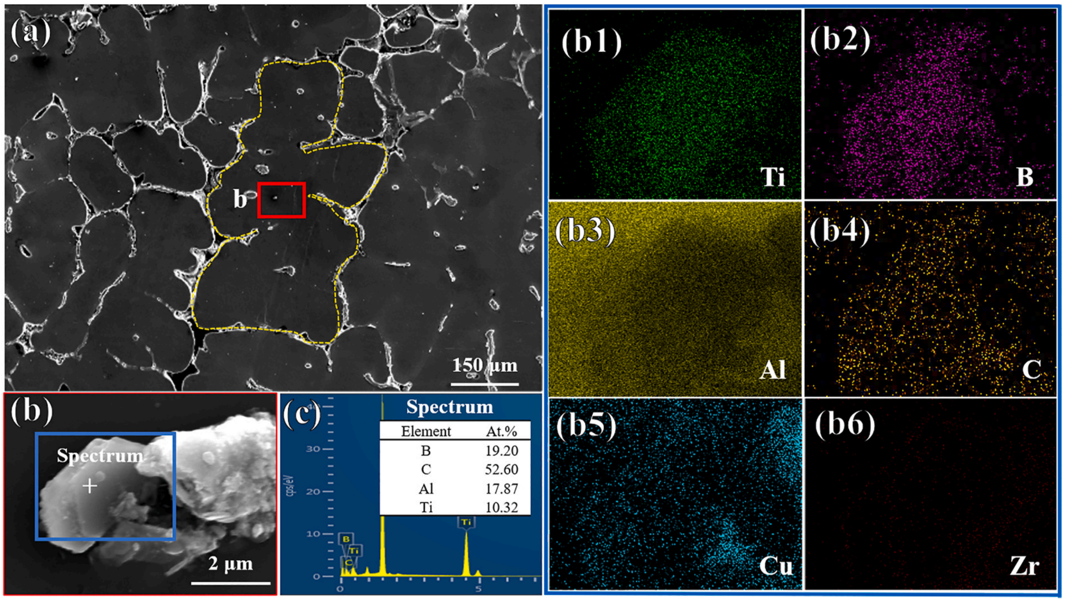

Element	At.%
B	19.20
C	52.60
Al	17.87
Ti	10.32

Fig. 5. Microstructure of the 2025-TCB alloys: (a) distribution of a typical B-doped TiC in grain center of α-Al; (b) magnified image of the B-doped TiC particle in (a); (b1-b6) the EDS results of Ti, B, C, Al, Cu and Zr elements in Fig. 5b; (c) the quantitative analysis of particle in Fig. 5b.

or coarse particles and is evenly dispersed throughout the Al matrix, with a streamlined alignment along the extrusion direction. The AlSiMn secondary phase consists primarily of tiny plates. These secondary phases in the 2025-TCB alloys change significantly after the T6 treatment, as shown in Fig. 7(d–f). The remaining coarse granular Al_2Cu secondary phase is spheroidized, partially decomposed and redissolved into the Al matrix while kept the streamlined distribution along the extrusion direction [51]. Conversely, the initial dot-like Al_2Cu secondary phase primarily decomposes and dissolves back into the matrix. The morphology of the AlSiMn secondary phase stays constant after T6 treatment due to its thermal stability. Previous studies have indicated that AlSiMn secondary phase is resistant to decomposition and dissolution into the Al matrix [52]. Fig. 7(a–c) also illustrate that as the Al-TCB master alloy content increased, the coarse Al_2Cu secondary phase disappeared, leaving only a dot-like Al_2Cu secondary phase. After T6 treatment, the number and size of remaining Al_2Cu secondary phase in the 2025 alloy decreased with the addition of Al-TCB master alloy, as shown in Fig. 7(d–f). The decrease in the number and the size of the remaining Al_2Cu second phase can also slightly enhance the mechanical properties to some extent. Thus, the addition of Al-TCB master alloy not only refined the matrix grains, but also influence the morphologies of Al_2Cu secondary phase in the matrix. However, due to the trace addition of Al-TCB master alloy, the enhancement value of the mechanical property is limited.

The microstructures of as-extruded and T6-treated 2025-TCB alloys were characterized by EBSD, as shown in Fig. 8. The black lines in the image represent grain boundaries with misorientation angles >15° (referred to as high angle grain boundaries, HAGBs). The unmarked areas in Fig. 8b correspond to the unidentified Al_2Cu secondary phase. As shown in Fig. 8(a–c), the as-extruded 2025 alloy primarily consists of coarse elongated grains. In contrast, the as-extruded 2025 alloys with 0.2 wt% and 2 wt% Al-TCB exhibit a combination of coarse elongated grains and fine equiaxed grains, displaying similar grain orientations. The matrix grains of the 2025 alloy with different Al-TCB master alloy additions were decreased even more during the extrusion process than the as-cast alloy due to the significantly plastic deformation applied, as shown in Fig. 8. During the extrusion process, the effect of applied large plastic deformation on the matrix grains is substantially greater than that of the Al-TCB master alloys. The average grain sizes of as-extruded samples are measured to 4.3 μm, 3.9 μm and 3.0 μm, respectively. The introduced B-doped TiC and C-doped TiB_2 particles are ceramic particles with high hardness and high elastic modulus. During the extrusion processing, these ceramic particles will also influence the grain structure by hindering the deformation and inhibiting grain growth to a certain extent [44,47,53]. Thus the grains of the 2025 after adding Al-TCB are slightly smaller than those without addition. After the T6 treatment, the grains of 2025 alloy recrystallized and grew, shifting from fine grains to coarse grains. Despite the increased average grain size, the grains remain elongated along the extrusion direction. T6 treatment resulted in larger average grain sizes (508.5 μm, 479.1 μm and 433.6 μm, respectively). The introduced B-doped TiC and C-doped TiB_2 particles effectively inhibit the growth of α-Al to some extent during the T6 process.

Fig. 9 shows the recrystallization and substructure distribution of as-extruded and T6 treated 2025-TCB alloys. As shown in Fig. 9(a–c), the microstructure of 2025 alloy primarily consists of recrystallized grains and substructures after hot extrusion. This structure results from dynamic recovery and dynamic recrystallization caused by external heat and mechanical forces during the hot extrusion process. After T6 treatment, previously recrystallized grains grew further, resulting in the development of coarse grains and an increase in the proportion of substructure. The addition of Al-TCB master alloy effectively inhibits grain growth, allowing for further microstructural refinement.

Fig. 10 shows the statistics of HAGBs in the extruded and T6 treated 2025-TCB alloys. As shown in Fig. 10(a–c), the proportion of HAGBs in the extruded alloys increased from 31.5 % to 47.0 % with the addition of Al-TCB master alloy. The enhancement is attributed to the Al-TCB master alloy, which refines the grains and optimizes the microstructure. HAGBs possess higher interface energy, which effectively hinders dislocation movement during deformation, and play a crucial role in improving mechanical properties of the alloy. After the T6 treatment, the proportion of HAGBs in the 2025 alloy remained above 40 %. Notably, the percentage of HAGBs in the 2025-TCB alloy exceeds than that of the 2025 base alloy. It is suggested that the addition of the Al-TCB not only aids in grain refinement but also helps to maintain a favorable distribution of HAGBs, hence improving the mechanical properties of the alloy.

Fig. 11 shows TEM images of T6 treated 2025-TCB alloys. The numerous fine precipitates are observed along the $[110]_{Al}$ zone axis, as shown in Fig. 11(a–c). After the aging process, a large number of θ′-Al_2Cu nanoprecipitates were formed. The numerical densities of the

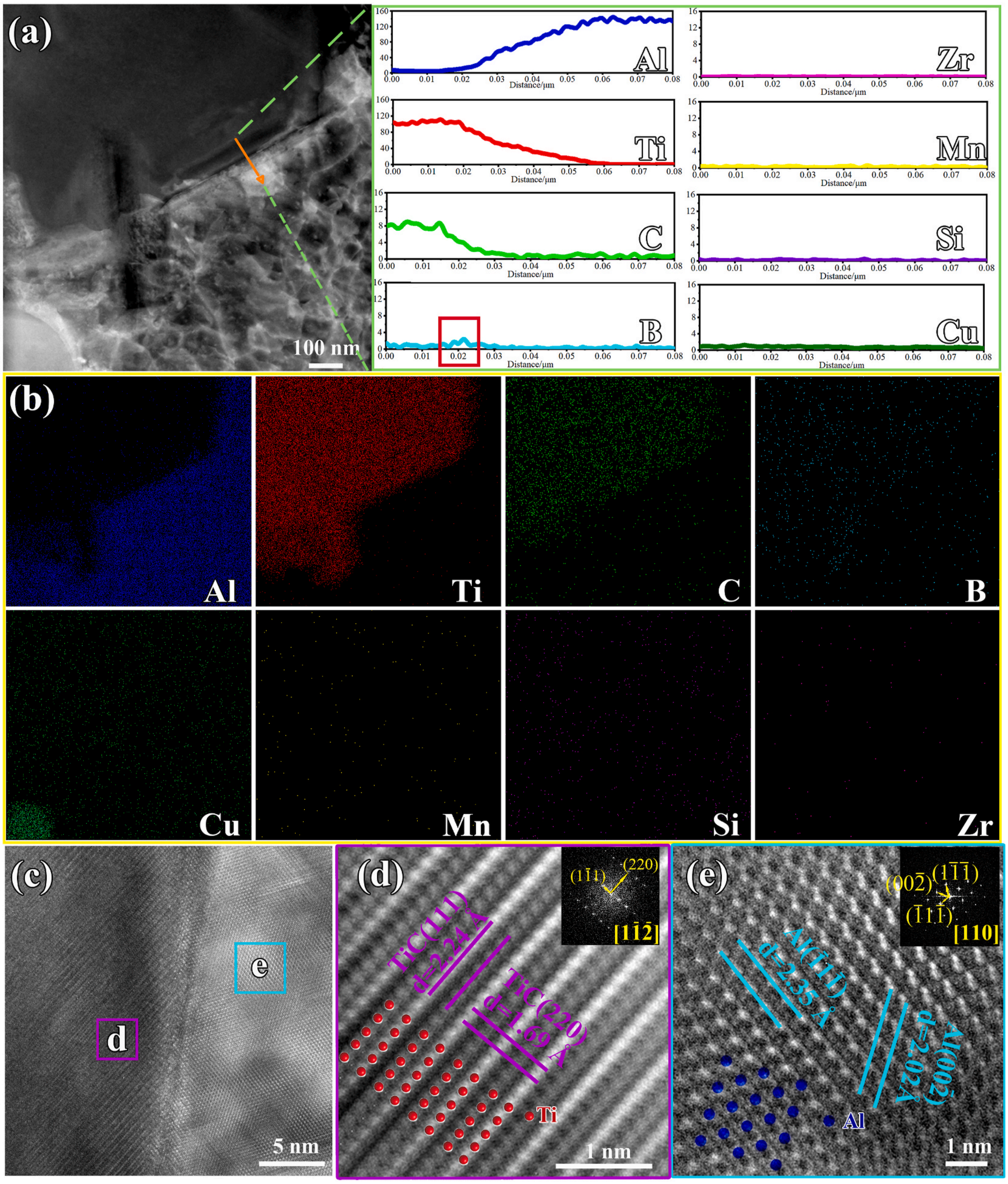

Fig. 6. HRTEM images of the B-doped TiC in 2025 ingot: (a) HADDF-STEM image and EDS line-scanning patterns of the B-doped TiC/Al interface; (b) EDS mapping of image (a); (c) HADDF image displaying the B-doped TiC/Al interface; (d, e) FFT images of the purple rectangle (B-doped TiC) and the blue rectangle (Al matrix) in image (c), respectively. (For interpretation of the references to colour in this figure legend, the reader is referred to the Web version of this article.)

θ′-Al_2Cu nanoprecipitates in 2025 base alloy, 2025-0.2 wt% Al-TCB alloy, and 2025-2 wt% Al-TCB alloy were calculated to be 2.0×10^{-3} nm^{-2}, 1.8×10^{-3} nm^{-2} and 2.2×10^{-3} nm^{-2} after T6 treatment, respectively. The average length of precipitates was 16.7 nm, 15.6 nm and 16.3 nm, respectively, with widths of less than 5 nm. The average length of θ′-Al_2Cu nanoprecipitates has been slightly reduced due to the refinement of the matrix grains [54]. In addition, no dislocations were observed. This absence can be explained by dislocation rearrangement after the longer aging times. Fig. 11d shows a magnified image of the 1.2 nm wide θ′-Al_2Cu precipitate. The inset in the upper right corner of Fig. 11d shows additional diffraction spots (marked by the yellow circles), which demonstrate the presence of the θ′-Al_2Cu precipitate.

Fig. 12 shows the engineering stress-strain curves for both as-extruded and T6 treated 2025-TCB alloys. As shown in the dashed line of Fig. 12a, the yield strength (YS) and ultimate tensile strength (UTS) of the as-extruded 2025 alloy are 115.7 MPa and 242.0 MPa, respectively, with a uniform elongation (EL) of 8.7 %. The UTS of the as-extruded 2025 alloy improves significantly as the Al-TCB master alloy content increases. The UTS of 2025-0.2 wt% Al-TCB and 2025-2 wt% Al-TCB alloys increase by 21.6 MPa and 22.3 MPa, respectively. At the same time, the EL of 2025-TCB alloys has increased. After T6 treatment, the YS and UTS of the 2025 alloy without Al-TCB and 2025-2 wt% Al-TCB alloy increase to 267.8 MPa, 383.8 MPa and 283.5 MPa, 400.0 MPa, respectively. It is noteworthy that the EL of both alloys has improved by around 20 %. The mechanical properties of as-extruded and T6 treated alloys have been presented in Table 4. The as-extruded 2025-TCB alloys exhibit an obvious Portevin-Le Chatelier (PLC) effect, as shown in Fig. 12a. It is attributed to the solid solution atoms within the Al matrix, which cause lattice distortion and suppressing dislocation motion [55]. However, it is noticed that the average YS of the 2025-0.2 wt% Al-TCB alloy decreased slightly from 267 MPa to 249 MPa compared to 2025 base alloy after T6 treatment. In general, the mechanical properties of

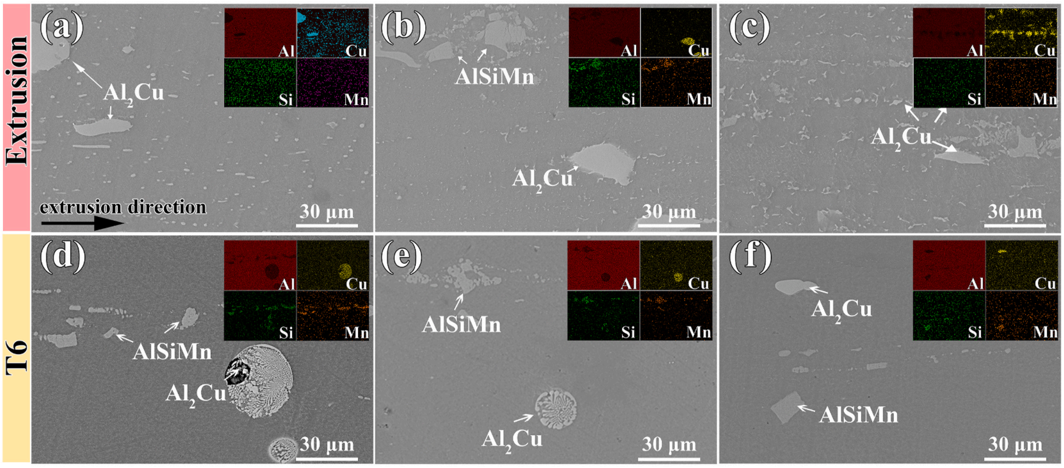

Fig. 7. Microstructure of the as-extruded and T6 treated 2025 alloys with and without Al-TCB: (a, d) 2025 base alloy; (b, e) adding 0.2 wt% Al-TCB; (c, f) adding 2 wt % Al-TCB.

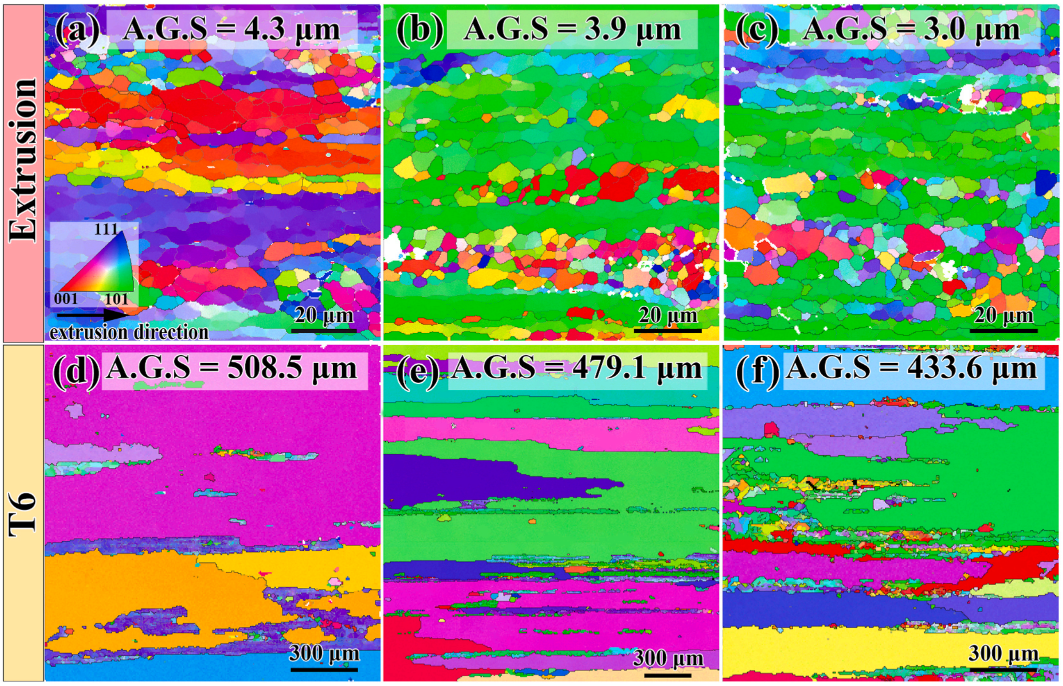

Fig. 8. EBSD maps of the as-extruded and T6 treated 2025 alloys with and without Al-TCB: (a, d) 2025 base alloy; (b, e) adding 0.2 wt% Al-TCB; (c, f) adding 2 wt% Al-TCB.

the alloy are related to the matrix grain size according to the Hall-Petch relationship. The yield strength of 2025-0.2 wt% Al-TCB alloy is expected to increase after the grain refinement of the matrix Al grains. However, the uniformity of microstructure and solid solution strengthening can not be ignored. When the Al-TCB addition content is 0.2 wt%, the optimization on grain size and secondary phase is not obvious, and some large Al_2Cu particles existed in some grains. After solution treatment, the non-uniform microstructure (Cu-rich and Cu-poor grains) may be formed due to the Al_2Cu secondary phase, with the strength of the two parts differing due to solution strengthening. When the load is applied, local stress concentration is easy to occur between Cu-rich and Cu-poor grains, which leads to the initiation and expansion of cracks, and finally decreases YS. When the addition of TCB is 2 wt%, the particles are more evenly distributed in the alloy and the grains and Al_2Cu secondary phases are fully refined. The fine equiaxed grain are formed in the alloy. After solution treatment, the non-uniformity microstructure and stress concentration are eliminated, and then both the YS and UTS of the alloy are improved. Further investigation will be carried out in our future work to reveal the exact cause. Fig. 12b shows true stress-strain curves for the 2025-TCB alloys, and the trend is consistent with engineering stress-strain curves. As shown in Fig. 12c, the strain hardening rate curves ($\Theta = d\sigma/d\varepsilon$) of 2025-TCB alloys drop fast as strain increases. In comparison to the T6 treated 2025-TCB alloys, two inflection points are observed in the strain hardening rate curve of extruded 2025-TCB alloys. The presence of the second inflection point is due to extra strain hardening produced by the hindrance of dislocation movement by solid solution atoms in the Al matrix. Comparing 2025-TCB alloy to other Al-Cu alloys, as shown in Fig. 12d, it is clear that the EL of the 2025-TCB alloy is approximately 50 %–100 % greater than that of conventional Al-Cu alloys. It emphasizes the beneficial impact of the Al-TCB master alloy in enhancing ductility. Furthermore, the strength-ductility synergy of the 2025-2 wt% Al-TCB alloy outperforms

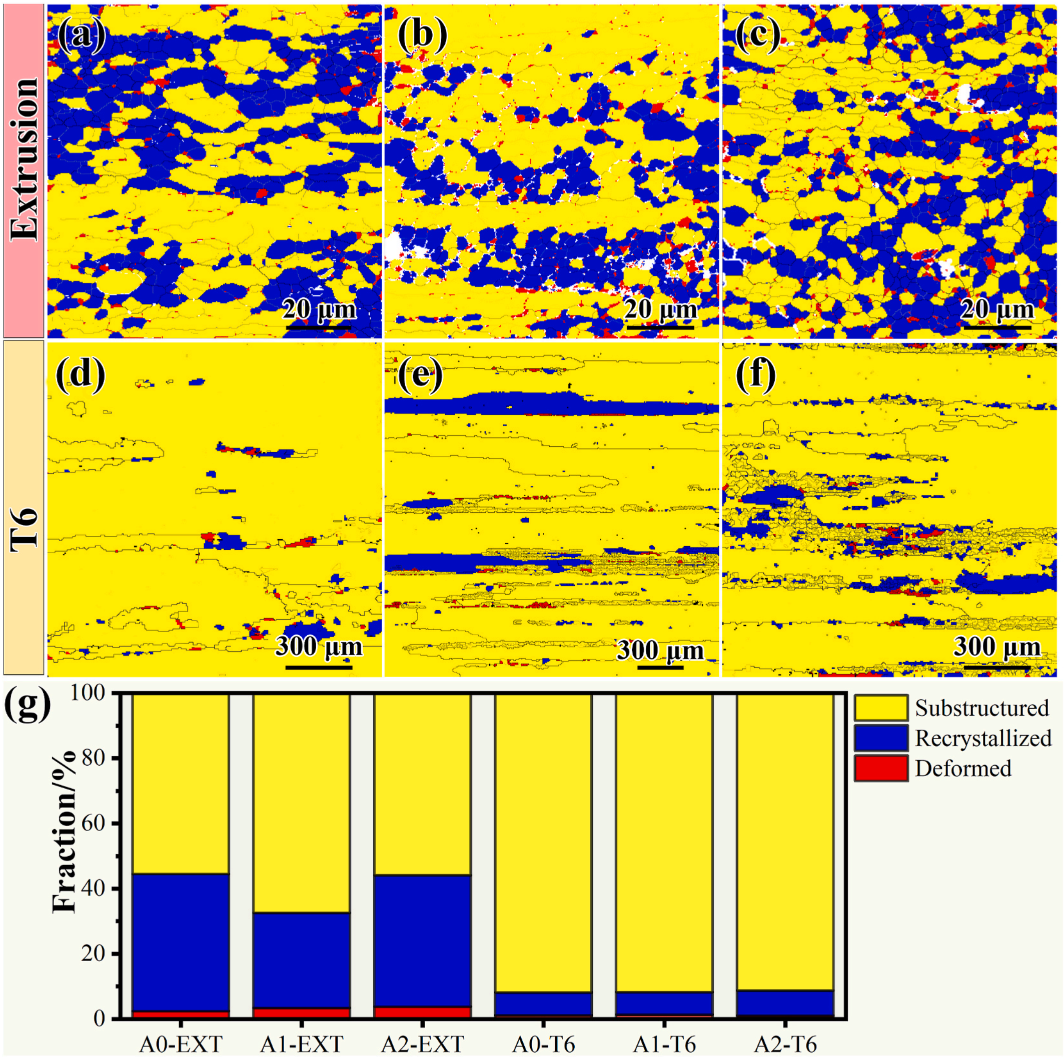

Fig. 9. Recrystallized distribution of the as-extruded and T6 treated 2025 alloys with and without Al-TCB: (a, d) 2025 base alloy; (b, e) adding 0.2 wt% Al-TCB; (c, f) adding 2 wt% Al-TCB; (g) recrystallization statistics of the as-extruded and T6 treated 2025 alloys.

that of previously reported Al-Cu alloys, showing the superior properties of the 2025-TCB alloy system.

4. Discussion

4.1. The effects of Al-TCB master alloy on grain refinement

Zr poisoning phenomena occurred in the aluminum containing Zr has been well known for the adverse effect of Zr on the grain refinement of traditional grain refiner such as Al-Ti-B master alloy. The effectiveness of Al-Ti-B master alloys can be dramatically reduced, resulting in a coarse and columnar grain structure in some cases [31,33]. It is a longstanding challenge to overcome the Zr poisoning problem completely for last decades. The Zr element in the melt is revealed to aggregate at the Al/TiB_2 interface at a concentration higher than 0.05 wt % and leads to the dissolution of the Al_3Ti formed on the TiB_2 surface during the grain refiner production process [31]. In our previous work, the Zr poisoning has also been proved in the Al-5Cu alloys with 0.1 % Zr, which lead to the coarse grain structure [35]. Efficiently refining α-Al grains in Zr-containing Al-Cu alloy (2025 alloy) is a significant challenge. In contrast, the Al-TCB master alloy containing B-doped TiC and C-doped TiB_2 particles can effectively serve as nucleation substrates of α-Al [35,40]. The incorporation of C atoms alters the physical and chemical properties of C-doped TiB_2, particularly reducing its ability to absorb Zr atoms on the surface of nucleated crystals. Meanwhile, the B-doped TiC eliminates the driving force for the reactions of the surface Zr atoms. As a result, both B-doped TiC and C-doped TiB_2 particles mitigate the effects of “Zr-poisoning” and promote the nucleation of α-Al. In this study, the grains are refined to 77 μm and Al_2Cu secondary phase receives a modified effect, as shown in Figs. 3 and 4. The grain refinement of 2025-TCB alloy is attributed to B-doped TiC in the Al-TCB master alloy, and the interface between B-doped TiC and Al matrix was characterized by HRTEM, as shown in Fig. 6. EDS examination confirms that there is no Zr element segregation at the interface of B-doped TiC and Al matrix, as shown in Fig. 6a and b. Furthermore, the results show that a good orientation relationship between B-doped TiC and Al. This makes B-doped TiC an efficient heterogeneous nucleation substrate for α-Al and refines the grains of the 2025 alloy.

4.2. Strengthening mechanism of the 2025-TCB alloys

In this study, the 2025-TCB alloy exhibits excellent mechanical properties. To comprehend superior properties, it is important to investigate the underlying strengthening mechanisms, which can be attributed to the following factors:

(a) Grain refinement

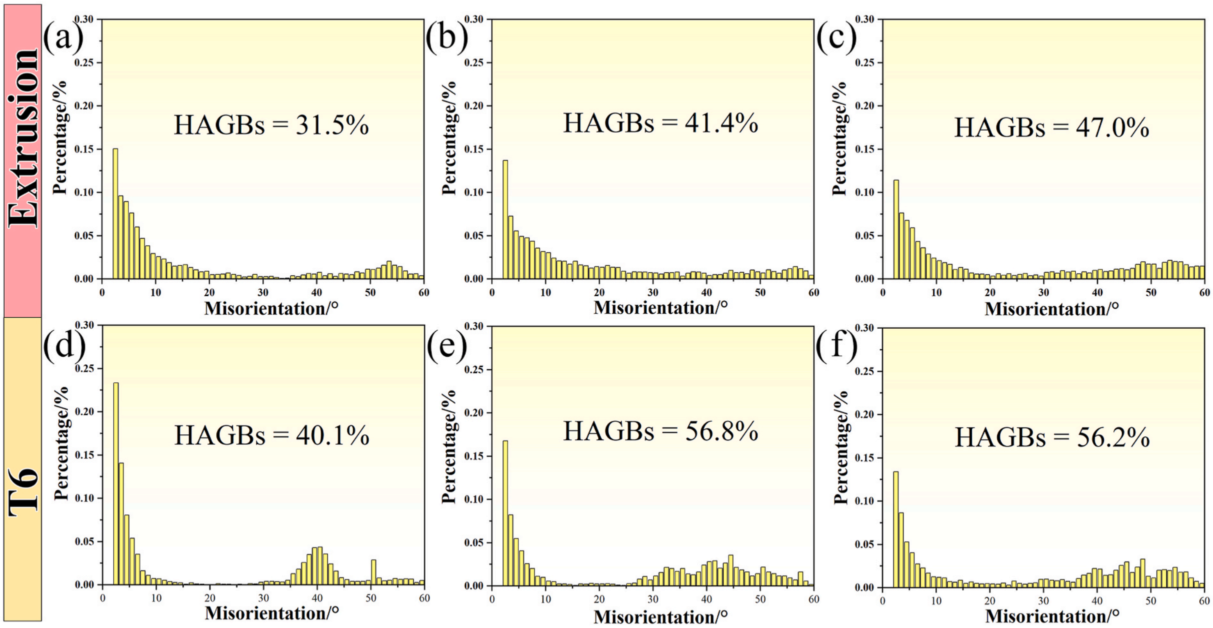

Fig. 10. Misorientation angles of adjacent grain boundaries of the as-extruded and T6 treated 2025 alloys with and without Al-TCB: (a, d) 2025 base alloy; (b, e) adding 0.2 wt% Al-TCB; (c, f) adding 2 wt% Al-TCB.

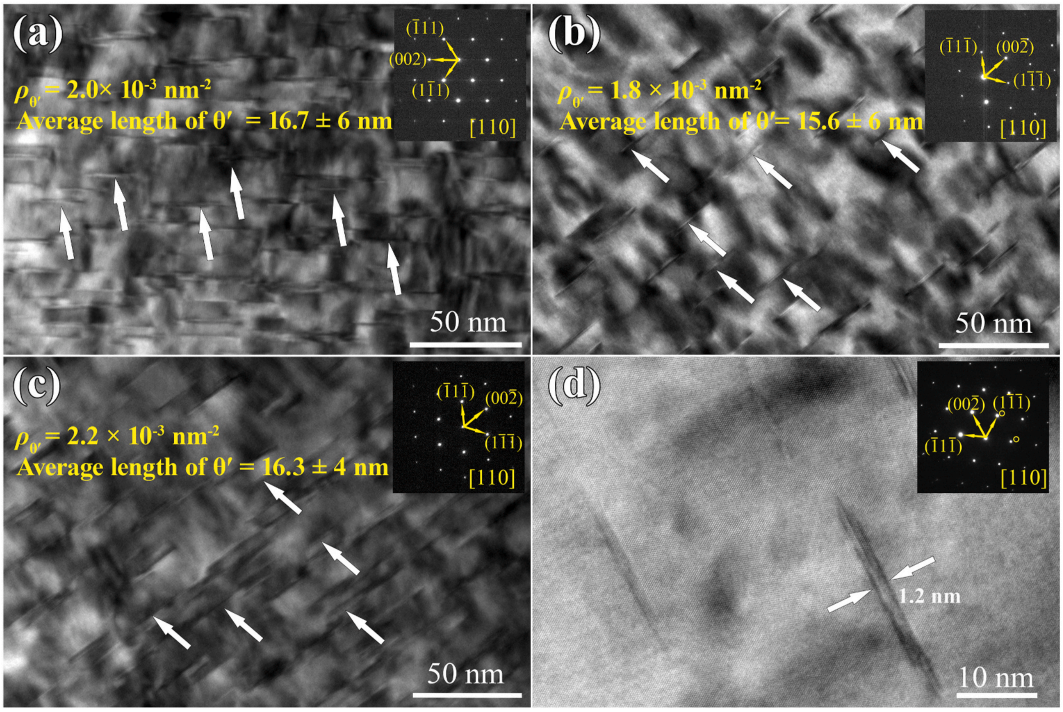

Fig. 11. TEM images of T6 treated 2025 alloys with and without Al-TCB: (a) 2025 base alloy; (b) adding 0.2 wt% Al-TCB; (c) adding 2 wt% Al-TCB. (d) θ′-Al_2Cu precipitates.

The effect of average grain size on the mechanical properties of metals can usually be described by the Hall-Petch relationship [51]:

$$\sigma_{GB} = \sigma_0 + \kappa d^{-1/2} \quad [2]$$

Where σ_{GB} is the yield strength, d is the average grain size, σ_0 and κ is the constant. The Hall-Petch relationship indicates that a smaller average grain size leads to an increase in yield strength. Due to the addition of the Al-TCB master alloy, the grains of as-cast 2025 alloy were refined and the microstructure and casting defects were optimized (see Fig. 3). Grains of 2025 alloy were finer after hot extrusion (see Fig. 8). During extrusion, these ceramic particles (B-doped TiC and C-doped TiB_2 in the Al-TCB master alloy) will influence the grain structure by hindering the deformation and inhibiting grain growth to a certain extent. Thus the grains of the 2025 alloy after adding Al-TCB are slightly smaller than those without. Finer grains provide more grain boundaries, which serve as obstacles to dislocation movement, enhancing the resistance to deformation and thus increasing the strength of the material.

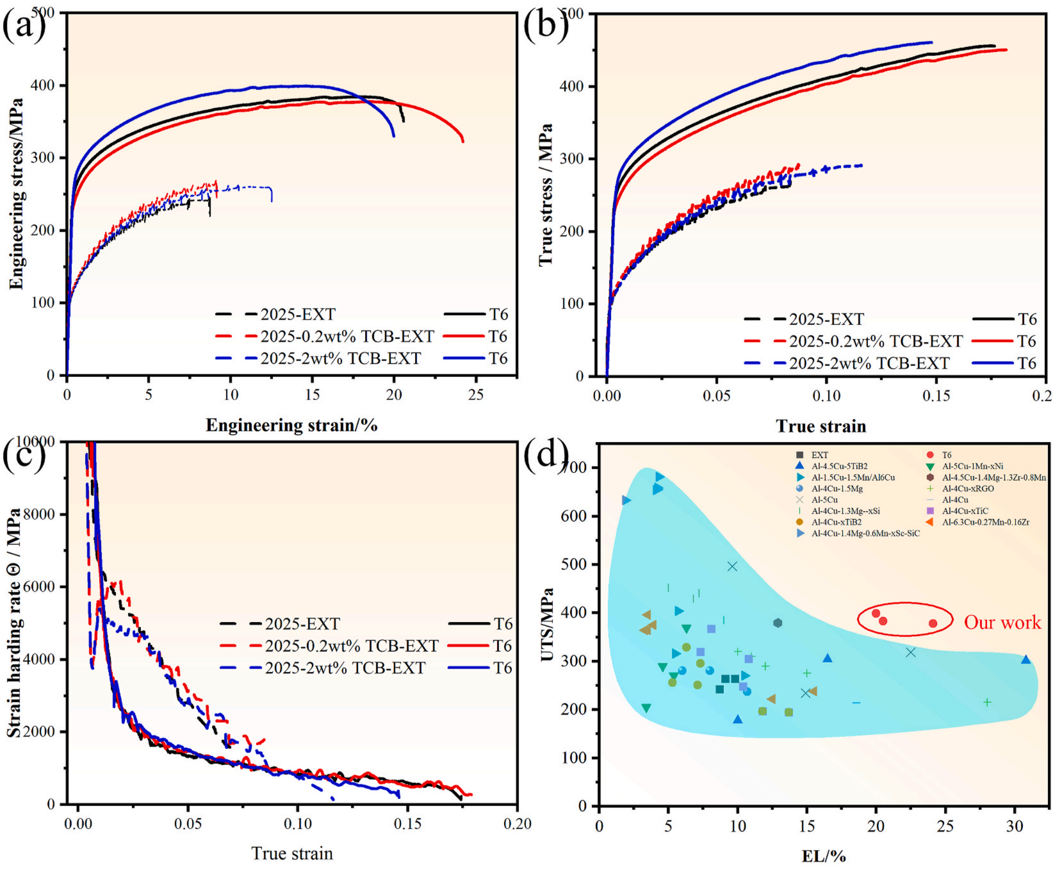

Fig. 12. Mechanical properties of the as-extruded and T6 treated 2025 alloys with and without Al-TCB: (a) engineering stress-strain curves; (b) true stress-strain curves; (c) strain-hardening curves; (d) comparison of the tensile properties for this work with other Al-Cu alloys [51,56–67].

Table 4
Mechanical properties at room temperature of the as-extruded and T6 treated 2025 alloys with and without Al-TCB.

States	Sample	YS (MPa)	UTS (MPa)	EL (%)
As-extruded	2025	115.7 ± 2.3	242.0 ± 5.0	8.7 ± 0.4
	2025-0.2 wt%- Al-TCB	120.5 ± 4.9	263.6 ± 3.6	12.4 ± 0.7
	2025-2 wt%- Al-TCB	115.2 ± 1.5	264.3 ± 4.5	9.1 ± 0.7
T6	2025	267.8 ± 3.4	383.8 ± 4.1	20.6 ± 0.7
	2025-0.2 wt%- Al-TCB	249.2 ± 8.4	378.1 ± 7.8	24.2 ± 0.2
	2025-2 wt%- Al-TCB	283.5 ± 1.1	400.0 ± 3.4	20.0 ± 1.5

(b) Precipitation strengthening

The strengthening of precipitates in Al-Cu alloy, particularly the θ′-Al_2Cu precipitate, is critical for enhancing the mechanical properties. The θ′-Al_2Cu precipitate increases the strength of the material by effectively obstructing the dislocation motion. According to the Orowan mechanism, the strengthening effect is described by Ref. [68]:

$$\sigma_{Orowan} = \frac{0.84MGb}{2\pi\lambda(1-\upsilon)^{1/2}} \ln\frac{2\bar{r}}{b} \qquad [3]$$

$$\lambda = \bar{r}\cdot\left(\frac{2\pi}{3\varphi_{AlCu_2}}\right)^{1/2} \qquad [4]$$

Where λ is the interspacing of particles; φ_{AlCu_2} is the volume fraction of precipitates and $\bar{r}$ is the average radius of the precipitates and other parameters are constants. The strength of the T6 treated alloy is enhanced with increasing the number of θ′-Al_2Cu precipitate and decreasing the average radius (see Fig. 11).

(c) Solid solution strengthening

The PLC effect observed in extruded 2025-TCB alloys (as shown in Fig. 12a) indicates that Cu、Mn、Si not only react with Al to form θ′-Al_2Cu and AlSiMn, but also dissolve in Al matrix. The solid solution of Cu、Mn、Si and Zr atoms causes lattice distortion and inhibits the dislocation movement, which can be described by Ref. [67]:

$$\sigma_{ss} = H\sum\nolimits_i C_i^n \qquad [5]$$

Where C_i is the concentration of i elements; H and n are constants. The concentration of elements can be analyzed by spectrum or EDS analysis (see Fig. 7).

(d) Dislocation strengthening

After extrusion, the dislocations within the Al matrix can impede the movement of newly formed dislocations, resulting in dislocation piling, which increases the strength of the alloys. Dislocation density usually decreases after T6 treatment. The effect of dislocation strengthening will be different between as-extruded and T6 treated alloys. The dislocation strengthening can be described by Ref. [69]:

$$\sigma_d = M\alpha Gb\rho_{GND}^{1/2} \qquad [6]$$

Where ρ_{GND} is the geometrically necessary dislocations (GNDs) density and other parameters are constant. The GNDs density can be calculated by the kernel average misorientation (KAM) that is retrieved directly

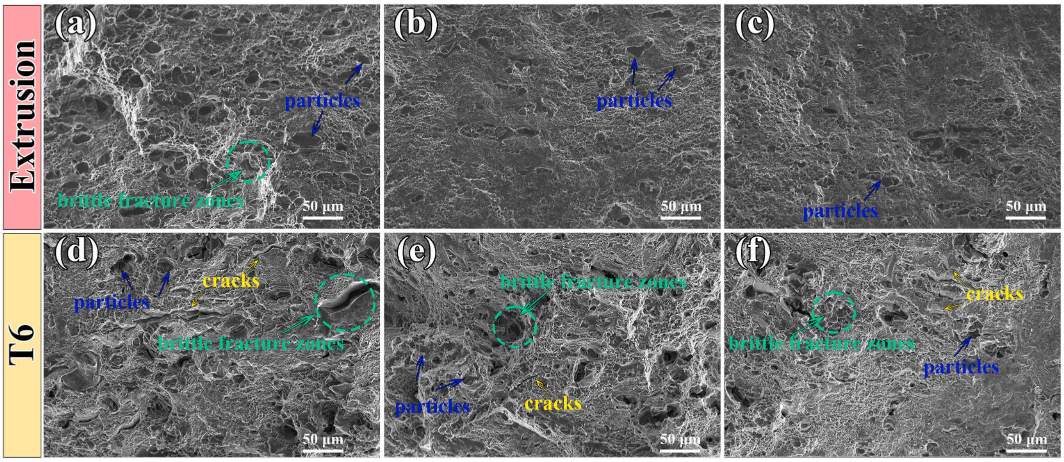

Fig. 13. The fractography of the as-extruded and T6 treated 2025 alloys with and without Al-TCB: (a, d) 2025 base alloy; (b, e) adding 0.2 wt% Al-TCB; (c, f) adding 2 wt% Al-TCB.

from the EBSD.

4.3. Tensile deformation behavior of the 2025-TCB alloys

Fig. 13 shows the fractography of the as-extruded and T6 treated 2025 alloys, both with and without Al-TCB. Notably, the fractography of T6 treated 2025-TCB alloys exhibits a considerably higher density of dimples than the extruded counterparts. Numerous dimples indicate that T6 treated 2025-TCB alloys can undergo more plastic deformation before failure. The fractography also reveals the presence of some particles within the Al matrix that match the AlSiMn and Al_2Cu secondary phases shown in Fig. 7. Secondary phase dispersion and micrometer size play an important influence in influencing the mechanical properties. Specifically, diffuse cracks and brittle fracture zones were observed in the fractography of T6 treated 2025-TCB alloys. It is indicated that stress concentrations may develop around these secondary phases, leading to crack initiation and propagation and eventually brittle fracture. Importantly, the addition of the Al-TCB master alloy to 2025 alloy has been shown to minimize the quantity and size of secondary phases, resulting in fewer cracks and brittle fracture zones.

5. Conclusion

In this work, the mechanism of grain refinement in a Zr-containing 2025 alloy refined with Al-TCB master alloy is revealed. Furthermore, the 2025-TCB alloys underwent extrusion and T6 treatment to improve their microstructure and mechanical properties. The main conclusions are as follows:

(1) As the Al-TCB content increased, the average grain size of a Zr-containing 2025 alloy decreased from 423 μm to 77 μm (from 0 wt% to 4 wt% Al-TCB), reaching up to 83 % reduction. The Al-TCB master alloy effectively refines the grains and overcomes Zr-poisoning.

(2) The B-doped TiC can act as an effective nucleation substrate for α-Al, possessing a suitable orientation relationship between them, where $[112]_{\text{B-doped TiC}}//[110]_{\alpha\text{-Al}}$; $(220)_{\text{B-doped TiC}}//(\bar{1}\,1\bar{1})_{\alpha\text{-Al}}$. The Zr has not aggregated at the interface of B-doped TiC/Al.

(3) Hot extrusion further refines the grain size of the 2025 alloy while optimizing the distribution and morphology of the Al_2Cu secondary phase. Both the grains and Al_2Cu secondary phase show a streamlined distribution along the extrusion direction. Notably, the incorporating the Al-TCB master alloy into 2025 alloy improves the morphology and distribution of the Al_2Cu secondary phase while retaining fine equiaxed grains. T6 treatment resulted in a high density of θ'-Al_2Cu nanoprecipitates in the Al matrix.

(4) Adding the Al-TCB master alloy to 2025 alloy significantly enhances its mechanical properties. 2025 Alloy with 2 wt% Al-TCB alloy had the best strength and ductility synergy. The UTS and EL of the extruded 2025-2 wt% Al-TCB alloy are 264.3 ± 4.5 MPa and 9.1 ± 0.7 %, respectively. The T6 treated 2025-2 wt% Al-TCB alloy has a UTS of 400.0 ± 3.4 MPa and an EL of 20.0 ± 1.5 %. The UTS of 2025-2 wt% Al-TCB alloy increases by 22.3 MPa and 16.2 MPa compared to the 2025 alloy without the Al-TCB after hot extrusion and T6 treatment.

(5) Strengthening effects mainly come from the microscopic level after extrusion and heat treatment, achieving uniform grain and precipitation distributions that obstacle dislocation movement. Lattice distortion induced by solid solution atoms also inhibited the dislocation movement.

CRediT authorship contribution statement

Zhan Liu: Writing – review & editing, Writing – original draft, Methodology, Investigation. **Jinfeng Nie:** Writing – review & editing, Supervision, Funding acquisition, Conceptualization. **Yuyao Chen:** Investigation. **Kaixuan Zhou:** Investigation. **Ruisheng Zhang:** Investigation. **Yonghao Zhao:** Supervision. **Chong Li:** Supervision. **Xiangfa Liu:** Supervision.

Declaration of competing interest

The authors declare that they have no known competing financial interests or personal relationships that could have appeared to influence the work reported in this paper.

Acknowledgement

This work is supported by the National Natural Science Foundation of China (Nos. U24A2026 and 52271033), Natural Science Foundation of Jiangsu Province, China (No. BK20221493), SEM, TEM and EBSD experiments are performed at the Materials Characterization and Research Center of Nanjing University of Science and Technology.

Data availability

All data included in this study are available upon request by contact with the corresponding author.

References

[1] H.W. Bai, Y.H. Gao, Y.J. Liu, X. Wu, P. Xu, J. Ma, F. Qian, X.C. Liu, Y.J. Li, Tailoring the microstructural hierarchy and strength-ductility synergy in a Mn-microalloyed Al-Cu alloy via a modified thermomechanical protocol, Mater. Sci. Eng., A 921 (2025) 147558.

[2] X. Su, Y. Lei, Y. Chen, H. Qu, Z. Qi, G. Zheng, X. Liu, H. Xiang, G. Chen, Precipitating thermally reinforcement phase in aluminum alloys for enhanced strength at 400 °C, J. Mater. Sci. Technol. 172 (2024) 71–82.

[3] J. Miao, C. Jiqiang, R. Jieke, L. Zhi, F. Zhenglin, Z. Zixiang, X. Ting, R, Guan, Wire-arc additive manufactured Al-Cu alloy: microstructure, mechanical properties and their anisotropy, Mater. Sci. Technol. 39 (2023) 2124–2134.

[4] R.E. Sanders, Technology innovation in aluminum products, JOM 53 (2001) 21–25.

[5] T.Y. Liu, J.S. Robinson, M.A. McCarthy, The influence of processing and microstructural parameters on the exfoliation corrosion susceptibility of 2025, Mater. Sci. Forum 396–402 (2002) 1419–1424.

[6] S. Kannan, S. Senthil Kumaran, L.A. Kumaraswamidhas, An investigation on compression strength analysis of commercial aluminium tube to aluminium 2025 tube plate by using TIG welding process, J. Alloys Compd. 666 (2016) 131–143.

[7] S. Kannan, S.S. Kumaran, L.A. Kumaraswamidhas, Optimization of friction welding by taguchi and ANOVA method on commercial aluminium tube to Al 2025 tube plate with backing block using an external tool, J. Mech. Sci. Technol. 30 (2016) 2225–2235.

[8] N.M. Kumar, S. Kannan, N. Mohanraj, L.A. Kumaraswamidhas, An experimental analysis of AA 2025 tube plate with commercial copper tube by gas tungsten arc welding, AIP Conf. Proc. 2283 (2020) 020034.

[9] F. Dong, Y. Yi, S. Huang, H. He, J. Huang, C. Wang, K. Huang, Refinement of second-phase particles and grain structures of 2219 AlCu alloy forgings using an improved thermomechanical treatment process, Mater. Char. 173 (2021) 110927.

[10] B. Li, Y. Shen, W. Hu, Casting defects induced fatigue damage in aircraft frames of ZL205A aluminum alloy - a failure analysis, Mater. Des. 32 (2011) 2570–2582.

[11] Y. Zhao, X. Lin, X. Rong, X. Zhang, D. Zhao, C. He, N, Zhao, Macro- and meso-mechanic investigations on the mechanical properties of heterostructured Al matrix composites featuring intragranular reinforcement, Mater. Res. Lett. 12 (2024) 408–416.

[12] M. Alipour, B.G. Aghdam, H.E. Rahnoma, M. Emamy, Investigation of the effect of Al-5Ti-1B grain refiner on dry sliding wear behavior of an Al-Zn-Mg-Cu alloy formed by strain-induced melt activation process, Mater. Des. 46 (2013) 766–775.

[13] X. Zhang, L. Li, Z. Wang, J. Gao, Z. Peng, Synergistic coupling of Mn-doped skeleton and Mg-toughened matrix: towards a heat-resistant Al-La-Mg-Mn alloy, Mater. Res. Lett. 12 (2024) 125–131.

[14] J. Xie, M. Lin, C. Xingpin, C. Yu, L. Wenjun, G, Huang, Strength-ductility synergy via cryogenic severe plastic deformation in an Al–Mg alloy achieved by clustering-induced strengthening, Mater. Res. Lett. 12 (2024) 373–380.

[15] K. Zhao, T. Gao, H. Yang, K. Hu, G. Liu, J. Nie, X. Liu, Strengthening behavior of B doped TiC particles on an Al–Zn–Mg alloy, Compos. Commun. 24 (2021) 100649.

[16] U. Bansal, M.P. Singh, S.K. Sinha, D.K. Sahu, S. Mondol, S.K. Makineni, A. Paul, K. Chattopadhyay, Strength and stability through variable micro segregation behaviour of Ta and Zr solutes at intermetallic interfaces in Al-Cu alloys, Acta Mater. 259 (2023) 119254.

[17] Y. Qi, H. Zhang, X. Yang, Y. Wang, C. Han, W. Fan, J. Liang, H. Zhu, Achieving superior high-temperature mechanical properties in Al-Cu-Li-Sc-Zr alloy with nano-scale microstructure via laser additive manufacturing, Mater. Res. Lett. 12 (2024) 17–25.

[18] Y. Geng, C. Zai, J. Yu, H. Tang, H. Lü, Z. Zhang, Strength and plasticity improvement induced by strong grain refinement after Zr alloying in selective laser-melted AlSiMg1.4 alloy, Trans. Nonferrous Metals Soc. China 34 (2024) 2733–2742.

[19] S.H. Seyed Ebrahimi, M. Emamy, N. Pourkia, H.R. Lashgari, The microstructure, hardness and tensile properties of a new super high strength aluminum alloy with Zr addition, Mater. Des. 31 (2010) 4450–4456.

[20] L. Ding, M. Zhao, F.J.H. Ehlers, Z. Jia, Z. Zhang, Y. Weng, D. Schryvers, Q. Liu, H. Idrissi, "branched" structural transformation of the L12-Al$_3$Zr phase manipulated by Cu substitution/segregation in the Al-Cu-Zr alloy system, J. Mater. Sci. Technol. 185 (2024) 186–206.

[21] Y. Chen, X. Chen, H. Chen, Y. Xiao, J. Dai, Y. Chen, Y. Cui, C. Dan, Z. Chen, X. Li, H. Wang, Abnormal grain growth in randomly-oriented fine grains in an Al-Mg-Sc-Zr alloy processed by laser-powder-bed-fusion, Mater. Res. Lett. 12 (2024) 635–643.

[22] S. Deng, J. Li, H. Ning, D. Lu, G. Zeng, Z. Liu, H. Xiang, J. Que, D. Liu, Effect of Zr addition on the microstructure evolution and mechanical properties of extruded Al-Cu-Li-Mn alloys, Mater. Char. 202 (2023) 113011.

[23] P.D. Willenshofer, M.A. Tunes, C. Kainz, O. Renk, T.M. Kremmer, S. Gneiger, P. J. Uggowitzer, S, Pogatscher, Precipitation behaviour in AlMgZnCuAg crossover alloy with coarse and ultrafine grains, Mater. Res. Lett. 11 (2023) 1063–1072.

[24] Y. Zhong, B. Zhang, L. Fang, J. Chen, W. Xu, X, Li, Giant hardening and formation of nanograined supersaturated solid solution in Al–Zn system, Mater. Res. Lett. 11 (2023) 764–771.

[25] X. Liu, Z. Wang, Z. Zhang, X. Bian, The relationship between microstructures and refining performances of Al-Ti-C master alloys, Mater. Sci. Eng., A 332 (2002) 70–74.

[26] J. Li, M. Huang, M. Ma, W. Ye, D. Liu, D. Song, B. Bai, H. Fang, Performance comparison of AlTiC and AlTiB master alloys in grain refinement of commercial and high purity aluminum, Trans. Nonferrous Metals Soc. China 16 (2006) 242–253.

[27] D.H. StJohn, M. Qian, M.A. Easton, P. Cao, The interdependence theory: the relationship between grain formation and nucleant selection, Acta Mater. 59 (2011) 4907–4921.

[28] Z. Fan, Y. Wang, Y. Zhang, T. Qin, X.R. Zhou, G.E. Thompson, T. Pennycook, T. Hashimoto, Grain refining mechanism in the Al/Al-Ti-B system, Acta Mater. 84 (2015) 292–304.

[29] D. Wu, S. Ma, T. Jing, Y. Wang, L. Wang, J. Kang, Q. Wang, W. Wang, T. Li, R. Su, Revealing the mechanism of grain refinement and anti Si-poisoning induced by (Nb, Ti)B2 with a sandwich-like structure, Acta Mater. 219 (2021) 117265.

[30] G. Mao, G. Tong, W. Gao, S. Liu, L. Zhong, The poisoning effect of Sc or Zr in grain refinement of Al-Si-Mg alloy with Al-Ti-B, Mater. Lett. 302 (2021) 130428.

[31] Y. Wang, C.M. Fang, L. Zhou, T. Hashimoto, X. Zhou, Q.M. Ramasse, Z. Fan, Mechanism for Zr poisoning of Al-Ti-B based grain refiners, Acta Mater. 164 (2019) 428–439.

[32] D. Qiu, J.A. Taylor, M.X. Zhang, Understanding the Co-Poisoning effect of Zr and Ti on the grain refinement of cast aluminum alloys, Metall. Mater. Trans. 41 (2010) 3412–3421.

[33] A.A. Rao, B.S. Murty, M. Chakraborty, Role of zirconium and impurities in grain refinement of aluminium lNith AI-Ti-B, Mater. Sci. Technol. 13 (1997) 769–777.

[34] J.A. Spittle, S. Sadli, The influence of zirconium and chromium on the grain-refining efficiency of Al-Ti-B inoculants, Cast Metals 7 (1995) 247–253.

[35] D. Li, X. Yan, Y. Fan, G. Liu, J. Nie, X. Liu, S. Liu, An anti Si/Zr-Poisoning strategy of Al grain refinement by the evolving effect of doped complex, Acta Mater. 249 (2023) 118812.

[36] W. Ding, W. Zhao, T. Xia, Grain refining action of Al-5Ti-C and Al-TiC master alloys with Al-5Ti master alloy addition for commercial purity aluminium, Int. J. Cast Metals Res. 27 (2014) 187–192.

[37] N. Frumin, N. Frage, M. Polak, M.P. Dariel, Wettability and phase formation in the TiC_xAl system, Scr. Mater. 37 (1997) 1263–1267.

[38] J. Nie, H. Ding, Y. Wu, X. Liu, Fabrication of titanium diboride-carbon core-shell structure particles and their application as high-efficiency grain refiners of wrought aluminum alloys, Scr. Mater. 68 (2013) 789–792.

[39] K. Zhao, T. Gao, H. Yang, G. Liu, Q. Sun, C. Wu, J. Nie, X. Liu, Influence of a new AlTiC-B master alloy on the casting and extruding behaviors of 7050 alloys, J. Alloys Compd. 820 (2020) 153089.

[40] H. Yang, Z. Qian, G. Zhang, J. Nie, X. Liu, The grain refinement performance of B-doped TiC on Zr-containing Al alloys, J. Alloys Compd. 731 (2018) 774–783.

[41] J. Nie, X. Liu, Y. Wu, The influences of B dopant on the crystal structure and nucleation ability of TiCx in the Al melt, Mater. Res. Bull. 48 (2013) 1645–1650.

[42] G. Li, X. Pan, H. Liao, J. Zheng, M. Yang, L. Qian, L. Lu, Sn-induced phase transformation mechanism from θ' to θ in Al-4Cu alloy and its influence on high temperature strength, Trans. Nonferrous Metals Soc. China 33 (2023) 2559–2573.

[43] G. Sha, L. Yao, X. Liao, S.P. Ringer, Z. Chao Duan, T.G. Langdon, Segregation of solute elements at grain boundaries in an ultrafine grained Al-Zn-Mg-Cu alloy, Ultramicroscopy 111 (2011) 500–505.

[44] B. Zhao, Q. Cai, J. Cheng, S. Yang, F. Chen, Microstructure and properties of as-cast Al-4.5Cu-1.5Mg alloy refined with Ti-supported TiC nanoparticles via ultrasonic-assisted addition, Mater. Sci. Eng., A 765 (2019) 138271.

[45] L. Ren, R. Tan, D. Zhang, X. Zhang, Regulating grain boundary element distribution of Al-Cu alloy to improve corrosion resistance by boron addition, Corros. Sci. 244 (2025) 112665.

[46] J. De Wilde, L. Froyen, S. Rex, Coupled two-phase [α(Al)+θ(Al2Cu)] planar growth and destabilisation along the univariant eutectic reaction in Al-Cu-Ag alloys, Scr. Mater. 51 (2004) 533–538.

[47] C. Zhang, W. Liao, Z. Shan, W. Song, X. Dong, Squeeze casting of 4032 aluminum alloy and the synergetic enhancement of strength and ductility via Al-Ti-Nb-B grain refiner, Mater. Sci. Eng., A 896 (2024) 146233.

[48] J.U. Rakhmonov, N.Q. Vo, J.R. Croteau, J. Dorn, D.C. Dunand, Laser-melted Al-3.6Mn-2.0Fe-1.8Si-0.9Zr (wt%) alloy with outstanding creep resistance via formation of α-Al(FeMn)Si precipitates, Addit. Manuf. 60 (2022) 103285.

[49] W. He, Y. Zhao, Q. Wei, H. Liu, D. Song, F. Shen, Z. Sun, R. Li, Effect of ultrasonic melt processing and cooling rate on microstructure evolution of Al-Cu-Mn-Mg-Fe-Si alloy, J. Mater. Res. Technol. 27 (2023) 3655–3669.

[50] N. Xiong, S. Friedrich, B. Friedrich, Purification of the Al2Cu intermetallic compound via zone melting crystallization technique, J. Mater. Res. Technol. 26 (2023) 973–983.

[51] R. Cui, L. Wang, Y. Su, B. Li, L. Yao, B. Wang, L. Luo, R. Chen, J. Guo, X. Tan, Multiscale microstructure containing nanometer-scale precipitations and stacking faults yields a high-strength Al-5Cu alloy by electron beam freeform fabrication, Acta Mater. 266 (2024) 119682.

[52] A. Biswas, D.J. Siegel, C. Wolverton, D.N. Seidman, Precipitates in Al-Cu alloys revisited: atom-Probe tomographic experiments and first-principles calculations of compositional evolution and interfacial segregation, Acta Mater. 59 (2011) 6187–6204.

[53] T.A. Davis, L. Bichler, F. D'Elia, N. Hort, Effect of TiBor on the grain refinement and hot tearing susceptibility of AZ91D magnesium alloy, J. Alloys Compd. 759 (2018) 70–79.

[54] G. Zeng, H. Li, B. Lin, P. Ma, X. Cai, S. Deng, H. Xiang, Z. Cai, J. Li, G. Xu, D. Liu, Influence of grain structure and precipitates on fatigue crack propagation behaviors of Al-xCu-1.2Li-X alloys, J. Alloys Compd. 1006 (2024) 176309.

[55] H. Jaber, B. Beausir, D. Entemeyer, T. Lebedkina, M. Novelli, M. Lebyodkin, Influence of surface pre-deformation on the Portevin-Le Chatelier effect and the related multiscale complexity of plastic flow in an Al-Mg alloy, Acta Mater. 279 (2024) 120330.

[56] J. Zhang, D. Zhang, H. Zhu, Z. Xie, In-situ TiB2 reinforced Al–4Cu matrix composites synthesized through microwave and conventional heating methods:

thermodynamics, dynamics and mechanical properties, Mater. Chem. Phys. 270 (2021) 124843.

[57] J. Zhang, D. Zhang, H. Zhu, Z. Xie, In-situ TiC reinforced Al-4Cu matrix composite: processing, microstructure and mechanical properties, Mater. Sci. Eng., A 794 (2020) 139946.

[58] F. Wang, Y. Zeng, B. Xiong, Y. Zhang, X. Li, Z. Li, H. Liu, Effect of Si addition on the microstructure and mechanical properties of Al-Cu-Mg alloy, J. Alloys Compd. 585 (2014) 474–478.

[59] X. Dong, Y. Guo, J. Wang, F. Xia, K. Ma, H. Duan, Z. Yang, P. Wang, M. Liang, J. Li, Novel AlCu solute cluster precipitates in the Al-Cu alloy by elevated aging and the effect on the tensile properties, Mater. Sci. Eng., A 862 (2023) 144454.

[60] M. Mandal, R. Mitra, Effect of pre-cold rolling on the evolution of microstructure, microtexture, and mechanical properties of the mushy state rolled in-situ Al-4.5Cu-5TiB$_2$ composite, Mater. Char. 146 (2018) 267–278.

[61] J. Chen, H. Liao, Y. Wu, H. Li, Contributions to high temperature strengthening from three types of heat-resistant phases formed during solidification, solution treatment and ageing treatment of Al-Cu-Mn-Ni alloys respectively, Mater. Sci. Eng., A 772 (2020) 138819.

[62] N.A. Belov, A.N. Alabin, I.A. Matveeva, Optimization of phase composition of Al-Cu-Mn-Zr-Sc alloys for rolled products without requirement for solution treatment and quenching, J. Alloys Compd. 583 (2014) 206–213.

[63] Y. Wang, X. Lin, Y. Zhao, Q. Wang, Z. Feng, H. Yang, W. Huang, Selective laser melted Al-Cu-Mg-Zr alloy with Ω-phase precipitation and excellent moderate-temperature tensile properties, Mater. Sci. Eng., A 861 (2022) 144368.

[64] Z. Qi, B. Cong, B. Qi, H. Sun, G. Zhao, J. Ding, Microstructure and mechanical properties of double-wire + arc additively manufactured Al-Cu-Mg alloys, J. Mater. Process. Technol. 255 (2018) 347–353.

[65] M. Khoshghadam-Pireyousefan, R. Rahmanifard, L. Orovcik, P. Švec, V. Klemm, Application of a novel method for fabrication of graphene reinforced aluminum matrix nanocomposites: synthesis, microstructure, and mechanical properties, Mater. Sci. Eng., A 772 (2020) 138820.

[66] J. Miao, J. Chen, X. Ting, W. Hu, J. Ren, T. Li, L. Zeng, R. Guan, O.A. Ojo, Effect of solution treatment on porosity, tensile properties and fatigue resistance of Al-Cu alloy fabricated by wire arc additive manufacturing, J. Mater. Res. Technol. 28 (2024) 1864–1874.

[67] Y. Cai, Y. Su, K. Liu, A. Hua, X. Wang, H. Cao, D. Zhang, Q. Ouyang, Effect of Sc microalloying on fabrication, microstructure and mechanical properties of SiCp/Al-Cu-Mg-Sc composites via powder metallurgy, Mater. Sci. Eng., A 877 (2023) 145152.

[68] M.E. van Dalen, D.C. Dunand, D.N. Seidman, Effects of Ti additions on the nanostructure and creep properties of precipitation-strengthened Al-Sc alloys, Acta Mater. 53 (2005) 4225–4235.

[69] K. Ma, H. Wen, T. Hu, T.D. Topping, D. Isheim, D.N. Seidman, E.J. Lavernia, J. M. Schoenung, Mechanical behavior and strengthening mechanisms in ultrafine grain precipitation-strengthened aluminum alloy, Acta Mater. 62 (2014) 141–155.